

Understanding the Origin of Highly Selective CO₂ Electroreduction to CO on Ni, N-doped Carbon Catalysts

David M. Koshy^(a), Shucheng Chen^(a), Dong Un Lee^(a), Michaela Burke Stevens^(a), Ahmed M. Abdellah^(b), Samuel M. Dull^(a), Gan Chen^(c), Dennis Nordlund^(d), Alessandro Gallo^(e), Christopher Hahn^(e), Drew C. Higgins^{*(b)}, Zhenan Bao^{*(a)}, Thomas F. Jaramillo^{*(a,e)}

Abstract: Ni, N-doped carbon catalysts have shown promising catalytic performance for CO₂ electroreduction (CO₂R) to CO; this activity has often been attributed to the presence of nitrogen-coordinated, single Ni atom active sites. However, experimentally confirming Ni-N bonding and correlating CO₂ reduction (CO₂R) activity to these species has remained a fundamental challenge. We synthesized polyacrylonitrile-derived Ni, N-doped carbon electrocatalysts (Ni-PACN) with a range of pyrolysis temperatures and Ni loadings and correlated their electrochemical activity with extensive physicochemical characterization to rigorously address the origin of activity in these materials. We found that the CO₂R to CO partial current density increased with increased Ni content before plateauing at 2 wt% which suggests a dispersed Ni active site. These dispersed active sites were investigated by hard and soft x-ray spectroscopy, which revealed that pyrrolic nitrogen ligands selectively bind Ni atoms in a distorted square-planar geometry that strongly resembles the active sites of molecular metal-porphyrin catalysts.

Introduction

The development of economically viable methods to produce carbon-neutral fuels and chemicals is essential for the realization of a sustainable energy economy.¹ Direct electrochemical reduction of carbon dioxide (CO₂) would help achieve this goal by utilizing renewable electricity to drive the production of value-added chemicals such as carbon monoxide, formate, ethylene, and ethanol.² Much of the work on the electrochemical reduction of CO₂ reduction (CO₂R) to date has focused on using transition metal surfaces that display selectivity for CO₂ conversion to a variety of C₁-C₃ products.^{3,4} Among these, carbon monoxide (CO) is a particularly desirable product because of its industrial usage

in the production of a wide variety of chemical products including phosgene, methanol, and aliphatic aldehydes.⁵ Synthesis gas, a mixture of CO and H₂, can also be used directly to produce liquid hydrocarbons in the gasoline and diesel range via the Fischer-Tropsch synthesis. Currently, most CO is produced from coal gasification or steam methane reforming; both methods relying on fossil fuels as the chemical feedstock.⁵ Thus, the electrochemical synthesis of CO from CO₂ would help provide a renewable route towards the precursors of many desirable commodity chemicals and fuels. A recent techno-economic analysis identified that large-scale electrochemical production of CO is a promising technology with positive projected economic value.⁶ These projections are based on estimates on the activity and selectivity of the electrocatalysts used for the CO₂ to CO conversion; thus, improving electrocatalytic performance is a strategy for improving the overall economics of CO₂ electrolysis. Currently, the most widely studied electrocatalysts for CO₂ electroreduction to CO are Ag and Au metallic surfaces.⁷ Despite the demonstrated performance of these catalysts, further catalyst discovery efforts are necessary to address the potentially prohibitive prices of these precious metal catalysts and to further improve the activity and selectivity of the catalysts in order to drive CO₂ electroreduction towards industrial relevance.

Heteroatom-doped graphitic carbon materials, particularly nitrogen-doped carbon (N-C), or metal and nitrogen doped carbon (M-N-C) catalysts are an exciting class of materials that are particularly well-suited for electrocatalytic applications due to their intrinsic electronic conductivity, low-cost, and high surface area. Importantly, these materials contain p-block elements, C and N, which perturbs the assumptions of the d-band model which has been shown to govern the intrinsic catalytic activity of metallic surfaces.⁸ Thus, the active sites in M-N-C catalysts hold promise for circumventing the limitations of metallic catalysts and achieving improved catalyst activity. This class of materials, particularly Fe-N-C, has already been shown to have high electrocatalytic activity for the oxygen reduction reaction (ORR) in acidic electrolytes.⁹⁻¹¹

In the CO₂ electroreduction literature, highly selective CO₂ reduction to CO has been reported by many groups for both N-C and M-N-C catalysts, with M = Fe, Co, and Ni showing the most promising performance.^{11,12} Among these materials, Ni-N-C has been reported by many groups to have Faradaic efficiencies toward CO exceeding 90%.¹³⁻²¹ The proposed active site structure for Ni-N-C is atomically dispersed Ni-N_x sites, a hypothesis that has been made based on evidence from electron microscopy,¹³ hard X-ray absorption spectroscopy,¹⁸ and density functional theory¹⁷. This active site determination closely matches the conclusions of the ORR literature for the Fe-N-C system where activity is attributed to FeN₄C_x sites that bear strong structure resemblance to typical molecular catalysts such as metal porphyrins and metal phthalocyanines.

- [a] D.M. Koshy, Dr. S. Chen, Dr. D.U. Lee, Dr. M.B. Stevens, S.M. Dull, Dr. Z. Bao, Dr. T.F. Jaramillo
SUNCAT Center for Interface Science and Catalysis, Department of Chemical Engineering
Stanford University, Stanford, CA 94305, USA
E-mail: zbao@stanford.edu, jaramillo@stanford.edu
- [b] A.M. Abdellah, Dr. D.C. Higgins
Department of Chemical Engineering
McMaster University, Hamilton, ON, Canada
E-mail: higgid2@mcmaster.ca
- [c] G. Chen
Department of Materials Science and Engineering
Stanford University, Stanford, CA 94305, USA
- [d] Dr. D. Nordlund
Stanford Synchrotron Radiation Lightsource
SLAC National Accelerator Laboratory, Menlo Park, CA 94025, USA
- [e] Dr. A. Gallo, Dr. C. Hahn
SUNCAT Center for Interface Science and Catalysis
SLAC National Accelerator Laboratory, Menlo Park, CA 94025, USA

RESEARCH ARTICLE

The Ni-N-C for CO₂R reports have, however, varied in their assignment of Ni oxidation state, coordination number, and bonding environment, and have not shown conclusive evidence of nitrogen-nickel bonding.¹³⁻²¹ In addition, previous reports have focused far more on characterizing Ni in the single atom form with less attention to the role of Ni aggregates in controlling the catalytic performance of Ni-N-C materials. Thus, open challenges remain in confirming that nickel-nitrogen bonding occurs in these materials, and in conclusively attributing catalytic activity to these dispersed Ni species.

To address this challenge, we tested a series of polymer-derived Ni-N-C catalysts synthesized through pyrolysis of polyacrylonitrile (PACN) particles and nickel nitrate at a range of Ni loadings and pyrolysis temperatures. PACN was synthesized directly from the acrylonitrile monomer in order to reduce metal contamination that is present in many commercial carbon materials such as carbon nanotubes, graphene, and graphite.

Through electrochemical CO₂ reduction testing, we show that Ni-PACN exhibits >95% selectivity to CO at electrode potentials between -0.7V and -1.1V vs RHE and that the partial geometric current density towards CO increases steadily with increased Ni catalyst loadings before plateauing at 14 mA/cm² at 2 wt% and higher Ni loadings. We showed that this CO₂ to CO conversion is unaffected by the appearance of Ni nanoparticles at high Ni loadings, although metallic Ni nanoparticles are expected to be active for the competing HER. We find that at sufficiently high pyrolysis temperatures (>700°C), Ni nanoparticles catalyze graphitization and are covered by carbon shells, which suppress the expected HER²² by restricting electrolyte access. We then propose that the plateau of partial current density towards CO provides electrokinetic evidence that dispersed Ni atoms are active sites for CO₂R. We used both hard (Ni K-edge) and soft x-ray (Ni L-edge and N K-edge) spectroscopic techniques to show that nickel-nitrogen coordination occurs in these materials, and that dispersed Ni atoms are likely coordinated to pyrrolic and pyridinic nitrogen ligands in a distorted square planar geometry. These findings demonstrate a direct link between homogeneous and heterogeneous catalysis as the dispersed Ni atoms are structurally similar to the pyrrolic nitrogen-coordinated metal centers in metal porphyrins. This combination of rigorous electrochemical testing and extensive physicochemical characterization clearly elucidates the origin of exceptional CO selectivity of Ni-N-C materials and can guide future catalyst design efforts for M-N-C-catalyzed CO₂ electroreduction.

Results and Discussion

Synthesis and Microscopy of Ni-PACN Electrocatalysts:

PACN-derived electrocatalysts were synthesized by a facile polymerization, oxidation, and pyrolysis procedure [Figure 1A, full experimental details in Supporting Information]. In brief, free-radical polymerization of acrylonitrile, initiated by azobisisobutyronitrile (AIBN), leads to formation of self-assembled flower-like superstructures as reported previously.²³ This step was performed with the addition of Ni salt in varying amounts to produce Ni-PACN catalysts with a distribution of Ni loadings. These polymer particles are stabilized by an oxidative

treatment at 230°C in air and subsequently pyrolyzed at 900°C in N₂ to produce the final Ni-PACN catalyst. The oxidative stabilization cyclizes and rigidifies the carbon framework which prevents the polymer from melting during high-temperature pyrolysis conditions, preserving the initial polymer particle morphology.

SEM imaging [Figures 1B, 1C] shows that the resulting catalysts have a nanostructured morphology which is insensitive to increased Ni weight loading as demonstrated in two representative samples, NiPACN-low (0.5 wt% Ni) and NiPACN-high (3.4 wt% Ni), with the final Ni weight loadings quantified in the final catalyst material by X-ray Fluorescence (XRF) spectroscopy. This shows that the assembly of the polymer superstructure is not strongly affected by the concentration of Ni(NO₃)₂ salt in the reaction solution. This result allows us to make fair catalytic comparisons between Ni-PACN catalysts with different Ni loading because activity differences are unlikely to stem from morphological differences between the catalysts.

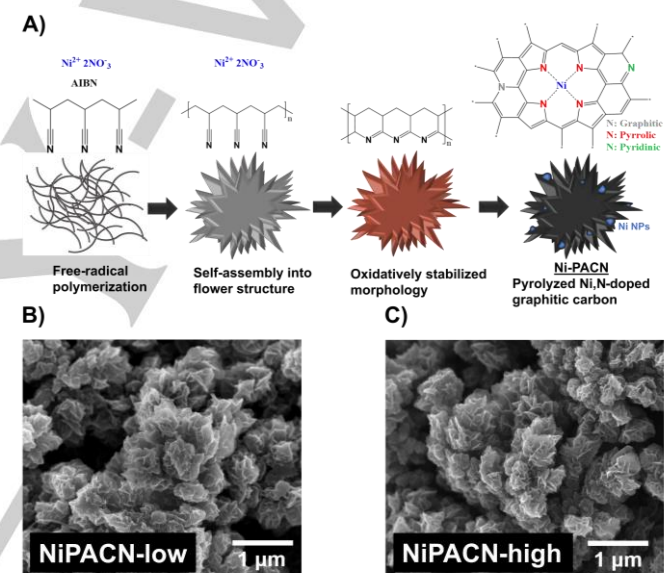


Figure 1. (A) Synthesis schematic shown for Ni-PACN. The final Ni-PACN structure containing a distribution of Ni nanoparticles (blue) and Ni-N-C sites (above molecular schematic shows hypothesized NiN₄ sites). SEM images of NiPACN-low (B) and NiPACN-high (C)

To further investigate the effect of Ni loading on the catalyst properties, STEM-HAADF imaging and EDS mapping of NiPACN-low and NiPACN-high was conducted [Figure 2]. By HAADF imaging, no Ni aggregates are evident on NiPACN-low, while high-contrast Ni-containing nanoparticles are present throughout the NiPACN-high structure. EDS mapping confirms the presence of Ni in both catalysts and shows that NiPACN-low contains uniformly distributed Ni signal, while NiPACN-high also contains Ni clusters corresponding to the nanoparticles observed by HAADF [Figure 2]. The color-intensity scaling of the NiPACN-high map makes it difficult to confirm the existence of dispersed Ni signal due to the high intensity aggregate regions but EDS maps of NiPACN-high taken in regions without aggregates show similar Ni signal to the NiPACN-low EDS map [SI Figure 2]. In

RESEARCH ARTICLE

both materials, EDS maps show a homogeneous distribution of nitrogen and oxygen dopants throughout the predominantly carbon matrix. We conclude that the primary effect of increasing Ni loading in Ni-PACN materials is the formation of Ni nanoparticles. Prior literature conclusively shows that Ni surfaces produce nearly exclusively hydrogen under CO₂ reduction conditions and their existence would be expected to reduce the selectivity of Ni-N-C catalysts for CO₂ reduction to CO.

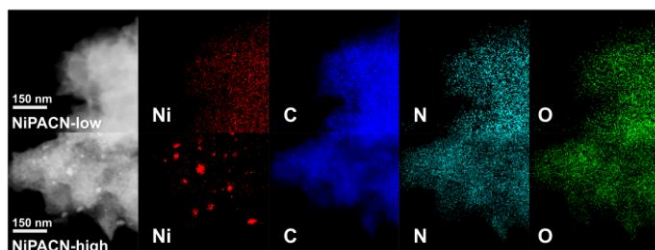


Figure 2. STEM-HAADF and EDS maps for Ni, C, N and O for NiPACN-low (top) and NiPACN-high (bottom).

CO₂ Electroreduction Performance

The catalytic performance of Ni-PACN for CO₂ electroreduction was assessed in a CO₂ vapor-fed, three-compartment electrochemical cell [SI Figure 1]. The NiPACN-low shows near-unity selectivity towards CO at electrode potentials between -0.7V and -1.1V vs RHE [Figure 3A]. This high selectivity is in agreement with many recent literature reports of selective CO production in Ni, N-doped carbon materials [summary of past reported Ni-N-C catalysts in SI Table 2].¹³⁻²¹ The partial current density towards CO increases with applied electrode potential and reaches 21 mA/cm² at -1.1V vs RHE before the onset of hydrogen evolution which results in a plateau in j_{CO} and an increase of j_{tot} to 40 mA/cm² at -1.3V vs RHE [Figure 3B]. We note that PACN, a Ni-free sample, produced negligible CO when tested at the same electrode potential which directly implicates Ni in the formation of the CO₂R active site [SI Figure 3].

To further investigate the electrochemical CO₂ reduction performance of Ni-PACN catalysts, we synthesized and tested a series of Ni-PACN with varying Ni contents. All catalysts were evaluated at -0.8V vs RHE to ensure that the current density would be below the transport-limited CO₂R current density of the cell, (estimated at ~20 mA/cm² from Fig 3B).

Figure 3C shows partial current densities towards CO (j_{CO}) plotted as a function of wt% Ni content in the catalyst. The j_{CO} of Ni-PACN rises with Ni content up to approximately 2 wt%, before plateauing at 14 mA/cm² with increasing amounts of Ni. This behavior indicates that catalytic activity is directly correlated to the Ni weight loading at low Ni loadings, but that above 2 wt% Ni the additional Ni does not create additional CO₂ reduction active sites.

Thus, the addition of dilute Ni to PACN produces a CO₂R active site while high Ni loadings lead to aggregates and no substantial change in catalyst activity; these observations represent electrokinetic evidence for a dispersed Ni active site.

Similar relationships between catalyst activity and metal loading have been used as evidence for dispersed active sites in the Fe-N-C system for ORR and WO_x-SiO₂ system for olefin metathesis.^{24,25} The nature of this dispersed active site is investigated thoroughly in the spectroscopic characterization section of this report and is shown to likely include nitrogen-coordinated Ni atoms in distorted square-planar geometries. We also note that the appearance of Ni aggregates at higher Ni loadings, as shown by EDS mapping, does not affect the CO₂ to CO current density which corroborates literature reports that metallic Ni does not appreciably catalyze CO₂R.²²

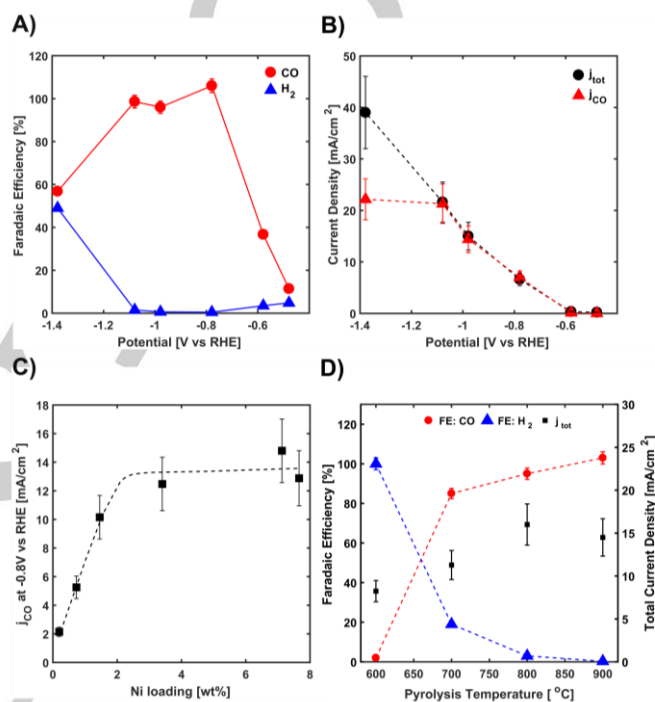


Figure 3. CO₂ reduction testing performed in a 3-compartment cell, 1 mg/cm² catalyst loading on Sigracet 39BC, and in 0.1M KHCO₃. (A) Faradaic efficiency to CO (red circles) and H₂ (blue triangles) on NiPACN-low as a function of electrode potential vs RHE (B) Corresponding total current density (black circles) and partial current density to CO (red triangles) for NiPACN-low. (C) Partial current density to CO at -0.8V vs RHE for a series of Ni-PACN catalysts with varying Ni loadings (synthesized by changing amount of Ni nitrate added in synthesis), Ni loadings measured by XRF. (D) Faradaic efficiency to CO (red circles) and H₂ (blue triangles) and current densities (black squares) at -0.8V vs RHE for NiPACN-high (3.4 wt% Ni) pyrolyzed at temperatures between 600°C and 900°C.

Finally, we found that NiPACN-high had a strong pyrolysis temperature dependence in which the CO selectivity and total current density decreased as the pyrolysis temperature was reduced below 900°C [Figure 3D]. At the lowest pyrolysis temperature of 600°C, NiPACN produced >99% H₂ — in stark contrast to the high CO selectivity of NiPACN-high pyrolyzed at (>700°C) high temperatures. This decreased selectivity implies the formation of a competing HER active site at low pyrolysis temperatures. This HER active site formation at reduced pyrolysis temperatures is also coupled with a decrease in total activity of the catalyst, which suggests that the optimal CO₂R active sites are also not formed at low pyrolysis temperatures. As NiPACN-

RESEARCH ARTICLE

high contains Ni aggregates, we hypothesize that the competing HER active site is related to the known predominance of HER under CO₂R conditions over metallic Ni surfaces. We note that double-layer capacitance measurements for these catalysts showed similar values which points to a comparable pore distribution and thus similar reactant diffusion in the Ni-PACN materials treated at different temperatures [SI Table 3]. This means that a change in the active site distribution is most likely responsible for this reversal in selectivity.

Effect of Ni aggregates on temperature-dependent Ni-PACN selectivity

We investigated the role of Ni aggregates in determining the temperature-dependent selectivity of NiPACN-high by XRD and TEM [Figure 4]. XRD patterns of NiPACN-high pyrolyzed at 600°C and 900°C and NiPACN-low pyrolyzed at 900°C were used to investigate the effect of pyrolysis temperature and Ni loading on the catalyst structure [Figure 4A]. Peaks corresponding to the graphite interlayer spacing at 3.4 Å, metallic Ni (111) at 2.03 Å and NiO (200) at 2.09 Å are observed in all materials. The graphitic interlayer spacing peak is broad on NiPACN-low which is representative of a disordered graphitic carbon lattice. The XRD pattern for NiPACN-high-900°C shows significant differences from the NiPACN-low XRD pattern; first, the metallic Ni and NiO peaks are higher intensity and more clearly resolved which agrees with the Ni aggregates observed by TEM. The graphitic interlayer spacing peak is narrow on NiPACN-high-900°C, which links Ni nanoparticles to enhanced graphitization on this material. We hypothesized that this graphitization was thermally activated and confirmed that, when NiPACN-high is pyrolyzed at 600°C, the distribution of graphite interlayer spacing is broad due to much reduced graphitization. These results show that the degree of graphitization of the stabilized polyacrylonitrile structure increases with both Ni loading and pyrolysis temperature.

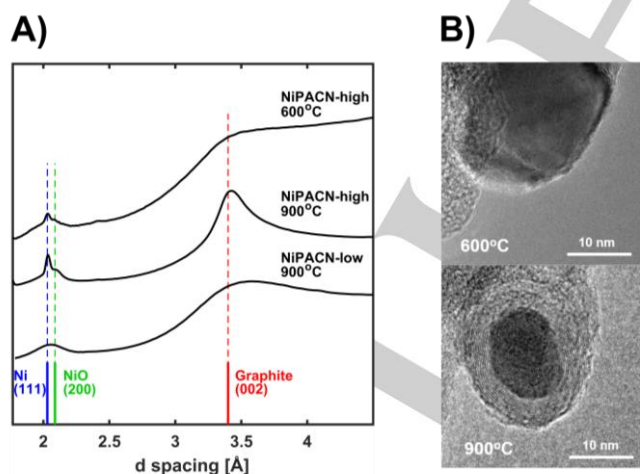


Figure 4. (A) XRD pattern for NiPACN-low-900°C, NiPACN-high-900°C, and NiPACN-high-600°C. (B) TEM images of the edge of nickel nanoparticles on NiPACN-high-600°C (above) and NiPACN-high-900°C (below).

Prior literature has found that the graphitization of amorphous carbon by Ni occurs only above 700°C, which corroborates the low degree of graphitization indicated by XRD of

NiPACN-high-600°C [Figure 4A].²⁶ The graphitization of carbon by Ni metal is hypothesized to occur via either a dissolution of carbon into Ni and subsequent precipitation as graphite, or by surface reactions of adsorbed carbonaceous species.²⁷ Both graphitization mechanisms produce graphitic carbon on top of Ni nanoparticles which forms a carbon shell around the nanoparticle that could restrict electrolyte access. This phenomenon has been observed in the Fe-N-C system for ORR.²⁸ We confirmed the existence of these carbon shells by TEM imaging of Ni nanoparticles in NiPACN-high pyrolyzed at 900°C and 600°C [Figure 4B]. For NiPACN-900°C, carbon layers can clearly be seen surrounding the Ni nanoparticle while for NiPACN-600°C the metal facet is left uncovered at the perimeter. Thus, the high temperature pyrolysis of Ni-PACN is essential for the Ni-catalyzed graphitization process that forms a carbon shell around the Ni nanoparticle and would likely restrict electrolyte accessibility to the Ni surface.

We hypothesize that the dependence of the CO selectivity of NiPACN-high on pyrolysis temperature stems from this Ni-catalyzed carbon shell formation. Particularly, at high pyrolysis temperatures, carbon shells hinder electrolyte access during electrochemical CO₂ reduction testing and render the nickel nanoparticles catalytically inactive. This phenomenon mitigates hydrogen evolution from occurring on the nickel surfaces, allowing for selective CO₂ reduction to CO on the catalyst driven by the dispersed Ni phase [Figure 3D]. At lower pyrolysis temperatures, the Ni-catalyzed graphitization is incomplete and exposes Ni surfaces to the electrolyte, resulting in predominantly hydrogen evolution occurring on the catalyst. Thus, the high temperature pyrolysis treatment plays a key role in slowing down H₂ evolution, facilitating the exceptional selectivity of Ni-N-C materials for CO₂ electroreduction to CO.

Spectroscopic Characterization of dispersed Ni and N in Ni-PACN Electrocatalysts:

As shown, the most likely active site for CO₂ electroreduction to CO are dispersed Ni species and not Ni aggregates. X-ray spectroscopic characterization of Ni-PACN was performed to elucidate the physicochemical structure of the highly dispersed nickel and nitrogen dopants to determine whether Ni-N coordinated species are present in Ni-PACN and could be responsible for the CO₂R activity. The samples "PACN" (Ni: 0 wt%), "NiPACN-low" (Ni: 0.5 wt%) and "NiPACN-high" (Ni: 3.4 wt%) were compared to show the effect of increased Ni content.

Nitrogen K-edge spectroscopy was used to precisely distinguish between different nitrogen defects to confirm the hypothesis of Ni binding to nitrogen atoms. [Figure 5A]. The 1s→π* transitions for metal-free PACN show peaks at 397.8 eV, 399.1 eV, and 400.6 eV which are attributed to pyridinic, pyrrolic, and graphitic nitrogen respectively.²⁹ Upon addition of Ni (NiPACN-low), the pyrrolic nitrogen peak grows substantially. These results suggest that Ni dopant atoms facilitate the formation of pyrrolic nitrogen sites, which they bind to selectively, resulting in increased absorption intensity at the pyrrolic resonant transition relative to metal-free PACN. This Ni-N_x moiety represents a direct parallel to molecular catalysts, particularly organometallic catalysts such as Ni-porphyrin and Ni-

RESEARCH ARTICLE

phthalocyanine which also bind Ni atoms through four pyrrolic nitrogen ligands.

At increased Ni loadings, the N K-edge XAS of NiPACN-high shows that the pyridinic and pyrrolic peaks have become convoluted and appear as a single broad peak at an intermediate value between the pyridinic and pyrrolic peaks, ~ 398 eV. We interpret the convolution of the peaks as evidence for increased heterogeneity in Ni-N coordination that occurs at high Ni loadings. At low loadings, the pyrrolic N functionalities coordinate Ni atoms resulting in a resolved pyrrolic nitrogen feature in NiPACN-low; at higher loadings, these optimal sites are saturated which causes a more heterogeneous distribution of Ni-N coordination that yields a convoluted pyridinic/pyrrolic peak for NiPACN-high.

XPS of the N1s region was used to support the hypothesis of Ni-N coordination in Ni-PACN [Figure 5B]. Based on the results of the N K-edge XAS, the XPS spectra were deconvoluted into three peaks; graphitic nitrogen at 401 eV, pyridinic nitrogen at 398.2 eV and an emergent peak with the addition of Ni in the pyrrolic nitrogen region ~ 399.5 eV [fitting parameters in SI Table 4].^{30–32} Pyrrolic nitrogen was not included in the metal-free PACN spectra because no improvement to the fit was obtained by the addition of this peak, further suggesting that the addition of Ni plays a strong role in forming these pyrrolic nitrogen defects. From XPS quantification, the total nitrogen content of the near-surface region of all three samples is high and rises with Ni content; 5.6 at% nitrogen for PACN; 7.6 at% nitrogen for NiPACN-low; and 7.7 at% nitrogen for NiPACN-high. The fraction of pyrrolic nitrogen relative to total nitrogen content increases with Ni loading, 12% for NiPACN-low to 24% for NiPACN-high which corroborates the results of the N K-edge XAS that pyrrolic nitrogen atoms likely coordinate Ni in NiPACN. This shift in the nitrogen functionality distribution shows that nickel plays a role in maintaining N-content during pyrolysis, likely driven by favorable thermodynamics of forming nitrogen-coordinated Ni species. This is supported by theoretical work that predicts that the binding energy of Ni atoms to a square-planar, pyridinic- N_4 site is as high as 8 eV.³³

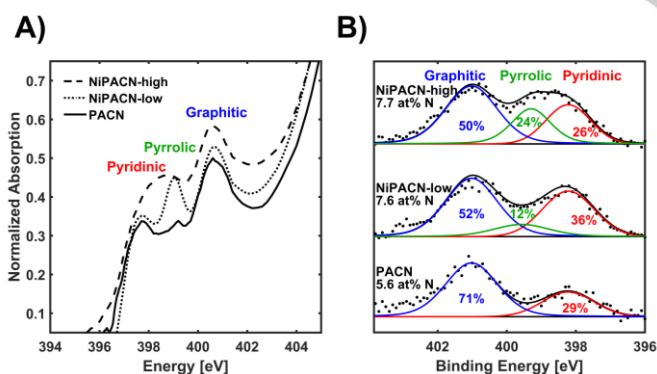


Figure 5. (A) Normalized N K-edge X-ray absorption spectra (B) N1s XPS spectra comparing fractions of graphitic (blue, left), pyrrolic (green, center) and pyridinic (red, right) defects with relative percentage of both peaks indicated.

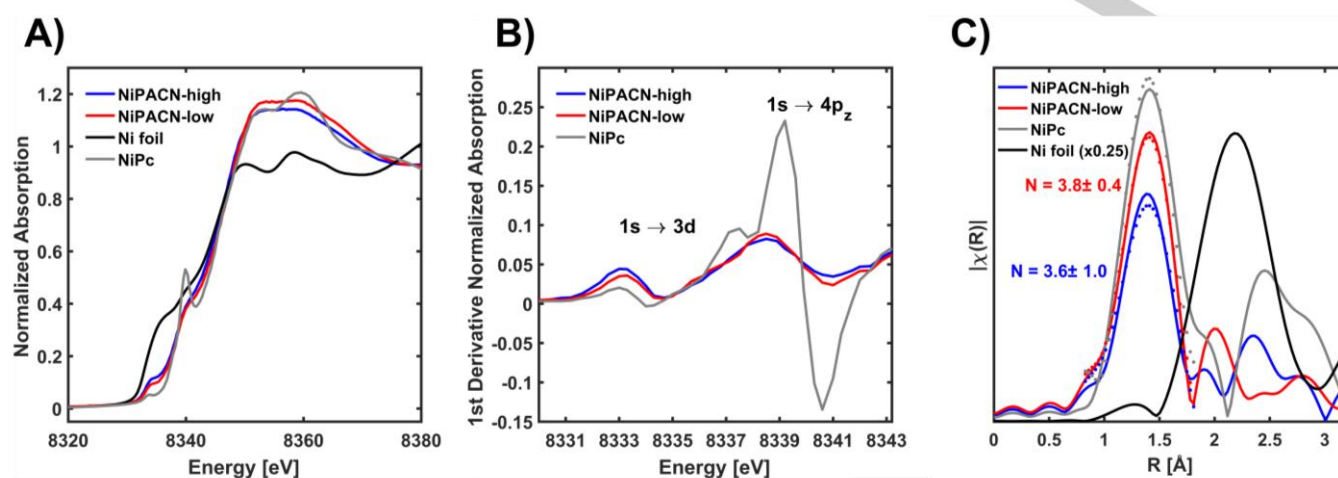
To characterize the chemical identity of the Ni atoms in the catalysts, we performed Ni K-edge X-ray absorption near edge structure (XANES) and extended X-ray absorption fine structure

(EXAFS) spectroscopy. The K-edge XANES spectra for NiPACN-low and NiPACN-high are compared to Ni foil and Ni phthalocyanine (NiPc) for reference [Figure 6A]. The edge location of the Ni-PACN samples is higher than for Ni foil and matches the Ni^{2+} atoms in NiPc, which shows oxidation of the Ni metal centers consistent with Ni L-edge spectroscopy and Ni XPS [SI Figure 5]. The XANES spectra of the Ni-PACN samples are both qualitatively similar to the NiPc spectra, implying geometric similarity between the Ni atoms in these samples. This similarity can be investigated further using the first derivative XANES spectra [Figure 6B], here the Ni foil spectra is omitted as metallic Ni has significantly different chemical composition than Ni-PACN and NiPc [1st derivative spectrum including all samples available in SI Figure 6]. Peaks at 8334 eV, corresponding to $1s \rightarrow 3d$ transitions, and at 8340 eV, corresponding to $1s \rightarrow 4p_z$ transitions, are evident on Ni-PACN samples and NiPc.³⁴ The $1s \rightarrow 3d$ transition at 8334 eV is significantly stronger in the Ni-PACN samples relative to NiPc, while the sharp $1s \rightarrow 4p_z$ transition of NiPc is reduced in the Ni-PACN [Figure 6B]. This $1s \rightarrow 3d$ transition is dipole-forbidden in centrosymmetric geometries, like square planar, which leads to a small feature for NiPc. The increased absorption intensity in Ni-PACN relative to NiPc suggests that the Ni environment is not uniformly centrosymmetric and thus deviates from the ideal square planar geometry.³⁵ Similarly, the characteristic sharp $4p_z$ transition of NiPc is significantly reduced in NiPACN, which is consistent with a distortion of the square planar NiPc geometry. A tetrahedral geometry was deemed inconsistent with the observed spectra as the existence of the $1s \rightarrow 4p_z$ peak in tetrahedral geometries is less prevalent and because the prominent bimodal post-edge, $1s \rightarrow 4p_x, 4p_y$ peak at ~ 8355 eV is present in square planar Ni complexes and not in tetrahedral Ni complexes.³⁵ Altogether, the Ni K-edge XANES results reveal that oxidized Ni atoms in a distorted square planar geometry are present in both NiPACN-high and NiPACN-low samples.

Ni K-edge EXAFS was collected to directly assess the coordination environment of the Ni atoms in Ni-PACN [Figure 6C]. The EXAFS of both Ni-PACN samples show a single prominent first shell peak at ~ 1.4 Å, which closely matches the Ni-N bonding location in NiPc. The fact that no higher shell contribution was detected in the EXAFS signal is consistent with the presence of mainly dispersed Ni sites. In particular, the absence of the peak at 2.2 Å in Ni-PACN (not phase shift corrected) for Ni-Ni scattering path in metallic Ni demonstrates that Ni metallic clusters are minority species in the Ni-PACN samples, while the absence of the second coordination shell peak at 2.5 Å in Ni-PACN (not phase shift corrected) is consistent with a higher disorder of the Ni sites in the Ni-PACN compared to the NiPc. Due to the similarity between NiPc and Ni-PACN, EXAFS fitting was performed to a square planar Ni-N model [SI Methods, SI Table 1, k-space fit shown in SI Figure 7] which resulted in a coordination number of 3.8 ± 0.4 and bond length of 1.876 ± 0.007 Å for NiPACN-low and a coordination number of 3.6 ± 1.0 and bond length of 1.885 ± 0.022 Å for NiPACN-high. These values support the existence of a four-coordinate square planar geometry for the Ni atoms suggested by XANES results. The error bars on the fitted coordination number increased from 0.5 in NiPACN-low to 1.1 in NiPACN-high and the error on the fitted bond length increased from 0.007 Å to 0.022 Å, which shows that at high Ni

loadings the Ni-N bonding configurations become more heterogeneous as shown in the N K-edge and N 1s XPS results. Similarly, the fitted Debye-Waller factors for NiPACN-low and

to NiPc value of 0.003 \AA^2 [SI Table 1]; this demonstrates higher disorder in Ni-PACN relative to the molecular NiPc sample and supports the hypothesized increase in heterogeneity in NiPACN-



NiPACN-high are 0.007 \AA^2 and 0.008 \AA^2 respectively compared high relative to NiPACN-low

Figure 6. (A) Normalized Ni K-edge X-ray absorption spectra (B) First-derivative of pre-edge region of spectra in (A) (C) EXAFS experimental data (full lines) of NiPACN-high, NiPACN-low, NiPc, and Ni foil and first-coordination shell fit (dotted lines) with fitted coordination number for NiPACN-low and NiPACN-high

We note that these Ni K-edge XANES and EXAFS results give a bulk-averaged picture of the Ni atoms in the Ni-PACN catalyst material and thus are sampling the full distribution of Ni coordination environments. This motivates future work using complementary methods to characterize the geometry and oxidation state of individual active sites in Ni-PACN to more precisely attribute CO_2R activity to specific NiN_x sites.

The combination of STEM-HAADF and STEM-EDS imaging, XRD, XPS, N K-edge XAS, Ni L-edge XAS, and Ni K-edge XANES and EXAFS was employed to thoroughly characterize the dispersed nickel species present in Ni-PACN materials that are the likely active sites for CO_2R to CO. The results indicate that dispersed, nitrogen-coordinated Ni atoms in a distorted planar geometry are present in both NiPACN-low and NiPACN-high and are preferentially bound by pyrrolic nitrogen atoms at low Ni loadings. These findings help rationalize the known activity of Ni phthalocyanine for CO_2R to CO³⁶ and are in-line with previous structure determinations of Ni-N-C materials.³⁷ Thus, a direct link between the structure and catalytic behavior of molecular macrocycle active sites and heterogeneous M-N-C catalyst systems has been demonstrated which motivates the use of molecular active site design principles in the development of heterogeneous catalysts.

Conclusion

Ni, N-doped carbon electrocatalysts (Ni-PACN) were synthesized by pyrolyzing polyacrylonitrile and nickel salts and tested for CO_2 reduction activity. In accordance with literature, Ni-PACN electrocatalysts exhibited greater than 95% selectivity to CO

between -0.7 and -1.1V vs RHE in a vapor-fed CO_2 reduction cell. We investigated the origin of this exceptional catalytic activity through electrochemical and physicochemical characterization of a series of Ni-PACN with varied Ni loadings and pyrolysis temperatures. Increasing Ni loading resulted in an increase in the partial current density to CO (j_{CO}) at an electrode potential of -0.8V vs RHE up until ~2 wt% Ni content, after which j_{CO} plateaus and Ni nanoparticles appear in the material as observed by STEM-HAADF and XRD. These observations are catalytic evidence for a dispersed Ni active site, which was investigated via hard and soft x-ray spectroscopy analysis at the Ni K and L-edges and the N K-edge. The spectroscopic results suggest that the active sites are pyrrolic coordinated-Ni atoms in a distorted square-planar geometry that is identical to Ni porphyrin, a typical molecular catalyst, which represents a direct analogy between heterogeneous and homogeneous catalysts. The assignment of CO_2 activity to dispersed Ni atoms and the confirmation of nickel-nitrogen binding analogous to molecular catalysts represent major advancements in our understanding of Ni-N-C catalysts and are necessary for further investigations into the catalytic cycle, spin state, and exact coordination environment of the catalytically active Ni centers. This thorough understanding of CO_2R on these materials will guide optimized Ni-N-C synthesis procedures that improve active site density and turnover frequency to produce promising electrocatalysts for economic conversion of CO_2 to CO.

Acknowledgements

This work is supported by the Joint Center for Artificial Photosynthesis, a DOE Energy Innovation Hub, supported

through the Office of Science of the US Department of Energy under Award no. DE-SC0004993. Part of this work was performed at the Stanford Nano Shared Facilities (SNSF), supported by the National Science Foundation under Award ECCS-1542152. Use of Stanford Synchrotron Radiation Lightsource, SLAC National Accelerator Laboratory is supported by the US Department of Energy, Office of Science, Office of Basic Energy Science, under Contract DE-AC02-76SF00515. STEM-HAADF imaging, along with EDS and EELS mapping carried out at the Canadian Centre for Electron Microscopy, a facility supported by the Canada Foundation for Innovation under the Major Science Initiative program, NSERC, and McMaster University.

Keywords: CO₂ Reduction • Metal, nitrogen doped carbon • Electrocatalysis • Heterogeneous Catalysis • X-ray absorption spectroscopy

- (1) Arakawa, H.; Aresta, M.; Armor, J. N.; Barteau, M. A.; Beckman, E. J.; Bell, A. T.; Bercaw, J. E.; Creutz, C.; Dinjus, E.; Dixon, D. A.; et al. Catalysis Research of Relevance to Carbon Management: Progress, Challenges, and Opportunities. *Chem. Rev.* **2001**, *101* (4), 953–996. <https://doi.org/10.1021/cr000018s>.
- (2) Chorkendorff, I.; Dickens, C. F.; Seh, Z. W.; Kibsgaard, J.; Jaramillo, T. F.; Nørskov, J. K. Combining Theory and Experiment in Electrocatalysis: Insights into Materials Design. *Science* (80-.). **2017**, *355* (6321), eaad4998. <https://doi.org/10.1126/science.aad4998>.
- (3) Hori, Y. *ELECTROCHEMICAL CO₂ REDUCTION ON METAL ELECTRODES*; 1385.
- (4) Kuhl, K. P.; Cave, E. R.; Abram, D. N.; Jaramillo, T. F. New Insights into the Electrochemical Reduction of Carbon Dioxide on Metallic Copper Surfaces. *Energy Environ. Sci.* **2012**, *5* (5), 7050–7059. <https://doi.org/10.1039/c2ee21234j>.
- (5) Bierhals, J. Carbon Monoxide. *Ullmann's Encycl. Ind. Chem. Vol. 6* **2012**, 565–582. <https://doi.org/10.1002/14356007.a05>.
- (6) Jouny, M.; Luc, W.; Jiao, F. General Techno-Economic Analysis of CO₂ Electrolysis Systems. *Ind. Eng. Chem. Res.* **2018**, *57* (6), 2165–2177. <https://doi.org/10.1021/acs.iecr.7b03514>.
- (7) Jovanov, Z. P.; Hansen, H. A.; Varela, A. S.; Malacrida, P.; Peterson, A. A.; Nørskov, J. K.; Stephens, I. E. L.; Chorkendorff, I. Opportunities and Challenges in the Electrocatalysis of CO₂ and CO Reduction Using Bifunctional Surfaces: A Theoretical and Experimental Study of Au–Cd Alloys. *J. Catal.* **2016**, *343*, 215–231. <https://doi.org/10.1016/j.jcat.2016.04.008>.
- (8) Gani, T. Z. H.; Kulik, H. J. Understanding and Breaking Scaling Relations in Single-Site Catalysis: Methane to Methanol Conversion by FeIV=O. *ACS Catal.* **2018**, *8* (2), 975–986. <https://doi.org/10.1021/acscatal.7b03597>.
- (9) Cullen, D. A.; Chung, H. T.; More, K. L.; Higgins, D.; Sneed, B. T.; Holby, E. F.; Zelenay, P. Direct Atomic-Level Insight into the Active Sites of a High-Performance PGM-Free ORR Catalyst. *Science* (80-.). **2017**, *357* (6350), 479–484. <https://doi.org/10.1126/science.aan2255>.
- (10) Kramm, U. I.; Lefèvre, M.; Larouche, N.; Schmeisser, D.; Dodelet, J. P. Correlations between Mass Activity and Physicochemical Properties of Fe/N/C Catalysts for the ORR in PEM Fuel Cell via ⁵⁷Fe Mössbauer Spectroscopy and Other Techniques. *J. Am. Chem. Soc.* **2014**, *136* (3), 978–985. <https://doi.org/10.1021/ja410076f>.
- (11) Zhang, J.; Xia, Z.; Dai, L. Carbon-Based Electrocatalysts for Advanced Energy Conversion and Storage. *Sci. Adv.* **2015**, *1* (7). <https://doi.org/10.1126/sciadv.1500564>.
- (12) Varela, A. S.; Ju, W.; Bagger, A.; Franco, P.; Rossmeisl, J.; Strasser, P. Electrochemical Reduction of CO₂ (CO₂RR) on Metal-Nitrogen-Doped Carbon (MNC) Catalysts. *ACS Catal.* **2019**. <https://doi.org/10.1021/acscatal.9b01405>.
- (13) Yi, C.; Zhao, S.; Li, H.; He, S.; Veder, J.-P.; Johannessen, B.; Xiao, J.; Lu, S.; Pan, J.; Chisholm, M. F.; et al. Unsaturated Edge-Anchored Ni Single Atoms on Porous Microwave Exfoliated Graphene Oxide for Electrochemical CO₂. *Appl. Catal. B Environ.* **2018**, *243* (June 2018), 294–303. <https://doi.org/10.1016/J.APCATB.2018.10.046>.
- (14) Su, P.; Iwase, K.; Nakanishi, S.; Hashimoto, K. Nickel-Nitrogen-Modified Graphene: An Efficient Electrocatalyst for the Reduction of Carbon Dioxide to Carbon Monoxide. **2016**, 6083–6089. <https://doi.org/10.1002/sml.201602158>.
- (15) Li, X.; Bi, W.; Chen, M.; Sun, Y.; Ju, H.; Yan, W.; Zhu, J.; Wu, X.; Chu, W.; Wu, C.; et al. Exclusive Ni – N 4 Sites Realize Near-Unity CO Selectivity for Electrochemical CO₂ Reduction. **2017**, 14889–14892. <https://doi.org/10.1021/jacs.7b09074>.
- (16) Yang, H. Bin; Hung, S.; Liu, S.; Yuan, K.; Miao, S.; Zhang, L.; Huang, X.; Wang, H.; Cai, W.; Chen, R.; et al. Atomically Dispersed Ni(i) as the Active Site for Electrochemical CO₂ Reduction. *Nat. Energy* **2018**, *3* (February). <https://doi.org/10.1038/s41560-017-0078-8>.
- (17) Yan, C.; Li, H.; Ye, Y.; Wu, H.; Cai, F.; Si, R. Coordinatively Unsaturated Nickel–nitrogen Sites towards Selective and High-Rate CO₂ Electroreduction. *Energy Environ. Sci.* **2018**. <https://doi.org/10.1039/C8EE00133B>.
- (18) Jiang, K.; Siahrostami, S.; Zheng, T.; Hu, Y.; Hwang, S.; Stavitski, E.; Peng, Y.; Dynes, J. J.; Gangishetty, M.; Su, D.; et al. Isolated Ni Single Atoms in Graphene Nanosheets for High-Performance CO₂ Reduction. *Energy Environ. Sci.* **2018**, 8–14. <https://doi.org/10.1039/C7EE03245E>.
- (19) Jeong, H. Y.; Balamurugan, M.; Choutipalli, V. S. K.; Jeong, E. S.; Subramanian, V.; Sim, U.; Nam, K. T. Achieving Highly Efficient CO₂ to CO Electroreduction Exceeding 300 mA Cm⁻² with Single-Atom Nickel Electrocatalysts. *J. Mater. Chem. A* **2019**, *7* (17), 10651–10661. <https://doi.org/10.1039/c9ta02405k>.
- (20) Yuan, C. Z.; Liang, K.; Xia, X. M.; Yang, Z. K.; Jiang, Y. F.; Zhao, T.; Lin, C.; Cheang, T. Y.; Zhong, S. L.; Xu, A. W. Powerful CO₂ Electroreduction Performance with N-Carbon Doped with Single Ni Atoms. *Catal. Sci. Technol.* **2019**, *9* (14), 3669–3674. <https://doi.org/10.1039/c9cy00363k>.
- (21) Mou, K.; Chen, Z.; Zhang, X.; Jiao, M.; Zhang, X.; Ge, X.; Zhang, W.; Liu, L. Highly Efficient Electroreduction of CO₂ on Nickel Single-Atom Catalysts: Atom Trapping and Nitrogen Anchoring. *Small* **2019**, *19*03668, 1–8. <https://doi.org/10.1002/sml.201903668>.

- (22) Kuhl, K. P.; Hatsukade, T.; Cave, E. R.; Abram, D. N.; Kibsgaard, J.; Jaramillo, T. F. Electrocatalytic Conversion of Carbon Dioxide to Methane and Methanol on Transition Metal Surfaces. *J. Am. Chem. Soc.* **2014**, *136* (40), 14107–14113. <https://doi.org/10.1021/ja505791r>.
- (23) S. Chen, D.M. Koshy, Y. Tsao, R. Pfattner, X. Yan, D. Feng, Z. B. Highly Tunable and Facile Synthesis of Uniform Carbon Flower Particles. *J. Am. Chem. Soc.* **2018**, *140* (32), 10297–10304. <https://doi.org/10.1021/jacs.8b05825>.
- (24) Lefèvre, M.; Dodelet, J. P.; Bertrand, P. O₂ Reduction in PEM Fuel Cells: Activity and Active Site Structural Information for Catalysts Obtained by the Pyrolysis at High Temperature of Fe Precursors. *J. Phys. Chem. B* **2000**, *104* (47), 11238–11247. <https://doi.org/10.1021/jp002444n>.
- (25) Lwin, S.; Li, Y.; Frenkel, A. I.; Wachs, I. E. Nature of WO_x Sites on SiO₂ and Their Molecular Structure-Reactivity/Selectivity Relationships for Propylene Metathesis. *ACS Catal.* **2016**, *6* (5), 3061–3071. <https://doi.org/10.1021/acscatal.6b00389>.
- (26) Yudasaka, M.; Tasaka, K.; Kikuchi, R.; Ohki, Y.; Yoshimura, S.; Ota, E. Influence of Chemical Bond of Carbon on Ni Catalyzed Graphitization. *J. Appl. Phys.* **1997**, *81* (11), 7623–7629. <https://doi.org/10.1063/1.365339>.
- (27) Presland, A. E. B.; Walker, P. L. Growth of Single-Crystal Graphite by Pyrolysis of Acetylene over Metals. *Carbon N. Y.* **2003**, *7* (1), 1–8. [https://doi.org/10.1016/0008-6223\(69\)90002-5](https://doi.org/10.1016/0008-6223(69)90002-5).
- (28) Gang Wu, 1 Karren L. More, 2 Christina M. Johnston, 1 Piotr Zelenay. High-Performance Electrocatalysts for Oxygen Reduction Derived from Polyaniline, Iron, and Cobalt. *Science (80-.)*. **2012**, *332* (2011), 443–447. <https://doi.org/10.1126/science.1200832>.
- (29) Jiang, H.; Gu, J.; Zheng, X.; Liu, M.; Qiu, X.; Wang, L.; Li, W.; Chen, Z.; Ji, X.; Li, J. Defect-Rich and Ultrathin N Doped Carbon Nanosheets as Advanced Trifunctional Metal-Free Electrocatalysts for the ORR, OER and HER. *Energy Environ. Sci.* **2019**, *12* (1), 322–333. <https://doi.org/10.1039/c8ee03276a>.
- (30) Kabir, S.; Artyushkova, K.; Kiefer, B.; Atanassov, P. Computational and Experimental Evidence for a New TM-N₃/C Moiety Family in Non-PGM Electrocatalysts. *Phys. Chem. Chem. Phys.* **2015**, *17* (27), 17785–17789. <https://doi.org/10.1039/c5cp02230d>.
- (31) Ferrandon, M.; Kropf, A. J.; Myers, D. J.; Artyushkova, K.; Kramm, U.; Bogdanoff, P.; Wu, G.; Johnston, C. M.; Zelenay, P. Multitechnique Characterization of a Polyaniline-Iron-Carbon Oxygen Reduction Catalyst. *J. Phys. Chem. C* **2012**, *116* (30), 16001–16013. <https://doi.org/10.1021/jp302396g>.
- (32) Susi, T.; Pichler, T.; Ayala, P. X-Ray Photoelectron Spectroscopy of Graphitic Carbon Nanomaterials Doped with Heteroatoms. *Beilstein J. Nanotechnol.* **2015**, *6* (1), 177–192. <https://doi.org/10.3762/bjnano.6.17>.
- (33) Yang, M.; Wang, L.; Li, M.; Hou, T.; Li, Y. Structural Stability and O₂ Dissociation on Nitrogen-Doped Graphene with Transition Metal Atoms Embedded: A First-Principles Study. *AIP Adv.* **2015**, *5* (6). <https://doi.org/10.1063/1.4922841>.
- (34) Feth, M. P.; Klein, A.; Bertagnolli, H. Investigation of the Ligand Exchange Behavior of Square-Planar nickel(II) Complexes by X-Ray Absorption Spectroscopy and X-Ray Diffraction. *Eur. J. Inorg. Chem.* **2003**, No. 5, 839–852. <https://doi.org/10.1002/ejic.200390114>.
- (35) Colpas, G. J.; Maroney, M. J.; Bagyinka, C.; Kumar, M.; Willis, W. S.; Suib, S. L.; Baidya, N.; Mascharak, P. K. X-Ray Spectroscopic Studies of Nickel Complexes, with Application to the Structure of Nickel Sites in Hydrogenases. *Inorg. Chem.* **1991**, *30* (5), 920–928. <https://doi.org/10.1021/ic00005a010>.
- (36) Shibata, M.; Furuya, N. Simultaneous Reduction of Carbon Dioxide and Nitrate Ions at Gas-Diffusion Electrodes with Various Metallophthalocyanine Catalysts. *Electrochim. Acta* **2003**, *48* (25–26), 3953–3958. [https://doi.org/10.1016/S0013-4686\(03\)00534-6](https://doi.org/10.1016/S0013-4686(03)00534-6).
- (37) Fei, H.; Dong, J.; Feng, Y.; Allen, C. S.; Wan, C.; Voloskiy, B.; Li, M.; Zhao, Z.; Wang, Y.; Sun, H.; et al. General Synthesis and Definitive Structural Identification of MN₄C₄ Single-Atom Catalysts with Tunable Electrocatalytic Activities. *Nat. Catal.* **2018**, *1* (1), 63–72. <https://doi.org/10.1038/s41929-017-0008-y>.

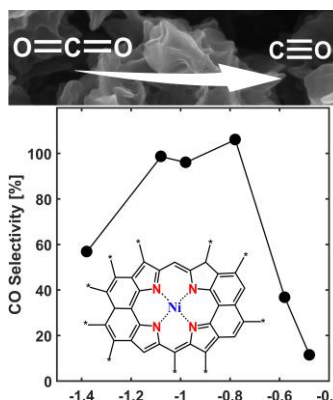
RESEARCH ARTICLE

Entry for the Table of Contents (Please choose one layout)

Layout 1:

RESEARCH ARTICLE

CO₂ electroreduction to CO has been shown to be catalyzed effectively by heteroatom-doped carbon materials but key insights into the catalytic active site are still unknown. Here, spectroscopic and kinetic characterizations are combined to identify nitrogen-coordinated, dispersed Ni atoms as the likely active sites for CO₂ to CO in Ni, N-doped electrocatalysts.



David M. Koshy, Shucheng Chen, Dong Un Lee, Michaela Burke Stevens, Ahmed M. Abdellah, Samuel M. Dull, Gan Chen, Dennis Nordlund, Alessandro Gallo, Christopher Hahn, Drew C. Higgins*, Zhenan Bao*, Thomas F. Jaramillo*

Page No. – Page No.

Understanding the Origin of Highly Selective CO₂ Electroreduction to CO on Ni, N-doped Carbon Catalysts